Across the tree of life, radiation resistance is governed by antioxidant Mn^{2+}, gauged by paramagnetic resonance

Ajay Sharma[a,1], Elena K. Gaidamakova[b,c,1], Olga Grichenko[b,c], Vera Y. Matrosova[b,c], Veronika Hoeke[a], Polina Klimenkova[b,c], Isabel H. Conze[b,d], Robert P. Volpe[b,c], Rok Tkavc[b,c], Cene Gostinčar[e], Nina Gunde-Cimerman[e], Jocelyne DiRuggiero[f], Igor Shuryak[g], Andrew Ozarowski[h], Brian M. Hoffman[a,i,2], and Michael J. Daly[b,2]

[a]Department of Chemistry, Northwestern University, Evanston, IL 60208; [b]Department of Pathology, Uniformed Services University of the Health Sciences, Bethesda, MD 20814; [c]Henry M. Jackson Foundation for the Advancement of Military Medicine, Bethesda, MD 20817; [d]Department of Biology, University of Bielefeld, Bielefeld, 33615, Germany; [e]Department of Biology, Biotechnical Faculty, University of Ljubljana, Ljubljana, SI-1000, Slovenia; [f]Department of Biology, Johns Hopkins University, Baltimore, MD 21218; [g]Center for Radiological Research, Columbia University, New York, NY 10032; [h]National High Magnetic Field Laboratory, Florida State University, Tallahassee, FL 32306; and [i]Department of Molecular Biosciences, Northwestern University, Evanston, IL 60208

Contributed by Brian M. Hoffman, September 15, 2017 (sent for review August 1, 2017; reviewed by Valeria Cizewski Culotta and Stefan Stoll)

Despite concerted functional genomic efforts to understand the complex phenotype of ionizing radiation (IR) resistance, a genome sequence cannot predict whether a cell is IR-resistant or not. Instead, we report that absorption-display electron paramagnetic resonance (EPR) spectroscopy of nonirradiated cells is highly diagnostic of IR survival and repair efficiency of DNA double-strand breaks (DSBs) caused by exposure to gamma radiation across archaea, bacteria, and eukaryotes, including fungi and human cells. IR-resistant cells, which are efficient at DSB repair, contain a high cellular content of manganous ions (Mn^{2+}) in high-symmetry (H) antioxidant complexes with small metabolites (e.g., orthophosphate, peptides), which exhibit narrow EPR signals (small zero-field splitting). In contrast, Mn^{2+} ions in IR-sensitive cells, which are inefficient at DSB repair, exist largely as low-symmetry (L) complexes with substantially broadened spectra seen with enzymes and strongly chelating ligands. The fraction of cellular Mn^{2+} present as H-complexes (H-Mn^{2+}), as measured by EPR of live, nonirradiated Mn-replete cells, is now the strongest known gauge of biological IR resistance between and within organisms representing all three domains of life: Antioxidant H-Mn^{2+} complexes, not antioxidant enzymes (e.g., Mn superoxide dismutase), govern IR survival. As the pool of intracellular metabolites needed to form H-Mn^{2+} complexes depends on the nutritional status of the cell, we conclude that IR resistance is predominantly a metabolic phenomenon. In a cross-kingdom analysis, the vast differences in taxonomic classification, genome size, and radioresistance between cell types studied here support that IR resistance is not controlled by the repertoire of DNA repair and antioxidant enzymes.

ionizing radiation | DNA repair | DSB | EPR | *Deinococcus*

Most, if not all, of the characteristics required for survival of life exposed to radiation are embodied by *Deinococcus radiodurans*, a nonsporulating bacterium capable of surviving doses of ionizing radiation (IR), X-rays and gamma rays (12–16 kGy), 10-fold greater than the yeast *Saccharomyces cerevisiae*, 20-fold greater than the bacterium *Escherichia coli*, and 3,000-fold greater than human cells (1). Despite concerted functional genomic efforts, the level of cellular IR resistance cannot be predicted by a genome sequence (1, 2). Without the identification of a distinct set of genes responsible for IR resistance, sequence-based approaches to gauging the wide range of radiosensitivities encountered in prokaryotes, simple eukaryotes, and even human-derived cancer cell lines have been futile (2–4). Indeed, genetic heterogeneity appears to be a central characteristic of IR resistance phenotypes in general (5, 6). Instead, it was long ago suggested that manganous ions (Mn^{2+}) accumulated in cells are responsible for extreme radiation resistance (7).

Reactive oxygen species (ROS) generated through the radiolysis of H_2O in cells subjected to IR are the primary molecular agents of cellular damage. In particular, irradiated cells rapidly form superoxide ($O_2^{\bullet-}$) ions by radiolytic reduction of both atmospheric O_2 and O_2 released through the intracellular decomposition of IR-generated H_2O_2 as catalyzed by both enzymatic and nonenzymatic metal ions. Importantly, because $O_2^{\bullet-}$ is charged, it cannot easily cross membranes and builds up in irradiated cells, selectively damaging proteins, not DNA (8). Nonenzymatic cellular mechanisms exist to resist superoxide damage. Notably, the IR-resistant bacterium *Lactobacillus plantarum*, which naturally lacks antioxidant enzymes, can efficiently convert high concentrations of IR-induced $O_2^{\bullet-}$ generated under anaerobic conditions back to membrane-permeable H_2O_2 ($O_2^{\bullet-} + 2H^+ \rightarrow H_2O_2$), which escapes irradiated cells. This intracellular reaction is catalyzed in *L. plantarum* by antioxidant low-molecular-weight (LMW) Mn^{2+} complexes (9–12). By comparison, the $O_2^{\bullet-}$-scavenging, manganese-dependent enzyme superoxide dismutase (MnSod) becomes increasingly less effective as a catalyst as concentrations of $O_2^{\bullet-}$ rise (13). This could explain why MnSod has repeatedly been shown to be dispensable for IR resistance in bacteria

Significance

Decades of functional genomic efforts have failed to predict the ability of cells to survive ionizing radiation (IR). Evidence is mounting that small high-symmetry antioxidant complexes of manganous ions with metabolites (H-Mn^{2+}) are responsible for cellular IR resistance, and that H-Mn^{2+} protects the proteome, not the genome, from IR-induced reactive oxygen species. We show that the amount of H-Mn^{2+} in nonirradiated living cells is readily gauged by electron paramagnetic resonance (EPR) spectroscopy and highly diagnostic of their DNA repair efficiency and survival after gamma-radiation exposure. This spectroscopic measure of cellular H-Mn^{2+} content is the strongest known biological indicator of cellular IR resistance between and within organisms across the three domains of the tree of life, with potential applications including optimization of radiotherapy.

Author contributions: A.S., E.K.G., B.M.H., and M.J.D. designed research; A.S., E.K.G., O.G., V.Y.M., V.H., P.K., I.H.C., R.P.V., R.T., C.G., J.D., and A.O. performed research; A.S., E.K.G., O.G., V.Y.M., V.H., C.G., N.G.-C., J.D., I.S., A.O., B.M.H., and M.J.D. analyzed data; and B.M.H. and M.J.D. wrote the paper.

Reviewers: V.C.C., Johns Hopkins University; and S.S., University of Washington.

The authors declare no conflict of interest.

This open access article is distributed under Creative Commons Attribution-NonCommercial-NoDerivatives License 4.0 (CC BY-NC-ND).

[1]A.S. and E.K.G. contributed equally to this work.

[2]To whom correspondence may be addressed. Email: bmh@northwestern.edu or michael.daly@usuhs.edu.

This article contains supporting information online at www.pnas.org/lookup/suppl/doi:10.1073/pnas.1713608114/-/DCSupplemental.

(7–10, 14, 15) and archaea (16), even though oxidative stress plays a major role in causing IR toxicity (8, 17).

The least frequent and most dangerous form of DNA damage caused by IR is the double-strand break (DSB). Impaired DSB repair currently provides the best available correlation with IR-induced cell death. Generally, any process that inhibits DSB repair, whether by mutation of repair genes or by ROS-mediated oxidative damage to repair enzymes, will severely limit a cell's ability to recover from IR. This is established, first, by the greatly increased radiosensitivity of specific DNA repair-deficient mutants (8). Second, evidence has mounted that oxidative protein damage is causative in IR toxicity, and antioxidant LMW complexes of Mn^{2+} with metabolites are the source of ROS protection in vivo (7–12, 18, 19). Such intracellular Mn antioxidants globally protect the proteome, and, logically, this must include DNA repair enzymes, from extreme oxidative assault during irradiation (5). Rationally designed *Deinococcus* Mn antioxidants display similar properties in vitro (19–21); they protect proteins from IR but not DNA or RNA, and are now used in the production of irradiated vaccines (22, 23) and as in vivo radioprotectors (24). Consistent with this focus on Mn^{2+} antioxidant complexes, we showed by absorption-display electron paramagnetic resonance (EPR) spectroscopy that the Mn^{2+} of *D. radiodurans* exists predominantly as high-symmetry (H) LMW complexes with phosphate, nitrogenous, and other metabolites, with no evidence for significant amounts of Mn^{2+} bound to MnSod (15).

IR-resistant *Deinococcus* bacteria accumulate high intracellular concentrations of H-Mn^{2+} complexes (15), which are also in high population in cell extracts (19). In contrast, H-Mn^{2+} complexes are largely absent in radiosensitive bacteria or their cell extracts (15, 19). LMW antioxidant protection has been identified as a critical component of IR resistance not only in bacteria and archaea (11, 16, 19) but also in a simple animal (bdelloid rotifer) (25). Two revelatory findings on the role of Mn antioxidants in protecting DNA repair enzymes are as follows: first, LMW cell extracts of IR-resistant, Mn-accumulating bacteria, but not from IR-sensitive cells, specifically protect proteins from severe oxidative damage in vitro during high-dose irradiations (5, 8, 11, 17–19), and, second, Mn antioxidants do not significantly influence IR-induced DSB yields across bacteria with greatly differing IR resistances and antioxidant statuses (5, 7). This disparity supports the hypothesis that proteins are the critical targets in IR-sensitive cells (5). However, the possibility that oxidative protein damage might also govern the functionality and efficiency of recovery of eukaryotes has not been explored (5).

We here report that in nutrient-replete cells with adequate supplies of Mn, it is not the amount of the cellular Mn^{2+}, and definitely not the action of MnSod, that controls the in vivo IR resistance; rather, it is the extent to which Mn^{2+} exists as H-complexes with LMW antioxidant metabolites: the Mn^{2+} speciation. This finding results from a combination of two approaches. First, we measure the IR resistance across prokaryotes and eukaryotes of differing genome sizes by evaluating the DSB repair efficiency in terms of the index, $DSBD_{10}$. This index represents the total number of DSBs generated per haploid genome when cells are irradiated by the IR dose (Gy) needed to kill 90% of the population, a survival index named D_{10} (5, 7). Second, we show that a simple measure of cellular Mn^{2+} speciation readily derived by absorption-display EPR spectroscopy of nonirradiated living cells (15, 26) correlates extremely well with $DSBD_{10}$ for irradiated cell types representing all three domains of life, and can be harnessed to gauge cellular IR resistance in an essentially "real-time" fashion and without exposure to IR. Thus, EPR may be suitable for gauging IR resistance of any cell type, with one potential application being the optimization of radiotherapy dose in patients who have cancer (6).

Results

IR Resistance. We determined survival (D_{10}) following gamma irradiation for a panel of cells from across the three domains of life: archaea; bacteria; and eukaryotes, including fungi and human cells. This panel incorporates eight *S. cerevisiae* strains with similarly sized genomes (10–14 Mbp) (Table 1 and *SI Appendix*, Fig. S1 *A* and *B*) from a collection of yeasts (*SI Appendix*, Table S1): two model laboratory strains (a haploid BY4741 and its diploid FY1679 counterpart), two MnSod-deficient mutants (Sod1 and Sod2) of strain BY4741, and four diploid environmental *S. cerevisiae* strains that were found to display significantly different IR resistances (Fig. 1, *Upper* and Table 1). We added the basidiomycete *Rhodotorula taiwanensis*, which is a moderately IR-resistant yeast with a larger genome (~20 Mbp). Under standard conditions for cell irradiation and pulsed-field gel electrophoresis (PFGE), we determined that the production of IR-induced DSBs for yeasts (BY4741, FY1679, EXF-6219, and EXF-6761) ranges between 0.0006 and 0.0009 DSB per mega-base pair per gray (DSB/Mbp/Gy) (*SI Appendix*, Fig. S1 *C* and *D*). We also examined nine bacterial strains [*D. radiodurans*, a *D. radiodurans* MnSod-deficient mutant (*sodA*$^-$), *Deinococcus ficus*, *Deinococcus geothermalis*, *Rubrobacter xylanophilus*, *E. coli*, *Pseudomonas putida*, *Enterococcus faecium*, and *Acinetobacter radioresistens*] with representatives previously characterized for IR-induced DSB yields by PFGE (7) and, similarly, for two archaea, *Halobacterium salinarum* and *Haloferax volcanii* (16). As a representative of mammalian cells, which are far more susceptible to IR-induced DSBs than prokaryotes and yeasts due to their massive genome size (~3 Gbp) (5, 27), we chose cultured Jurkat T cells. Jurkat cells are considered to be IR-resistant for human cells (D_{10}, 4 Gy) (28), but extremely IR-sensitive compared with prokaryotes and fungi, based on D_{10} (Table 1). For each of the cell types, we present the IR survival index, D_{10}, as well as the DNA repair efficiency index, $DSBD_{10}$, defined as $DSBD_{10} = [D_{10}\ (Gy)] \times [DSB\ Yield\ (DSB/Mbp/Gy)] \times [Genome\ size\ (Mbp)]$. This $DSBD_{10}$ index equals the number of DSBs inflicted per haploid genome at the IR dose that kills 90% of the population (Fig. 1, *Upper*). It corresponds to an irradiated cell's maximum survivable number of IR-induced DSBs, and reflects its efficiency in repairing the most lethal form of DNA damage: the DSB (5) (Table 1 and *SI Appendix*, Fig. S1 *C* and *D*).

The tabulated values of $DSBD_{10}$ for this cell panel (Table 1) indeed span the gamut of IR resistance. Thus, as we have described (5), the *D. radiodurans* strains are most efficient at DSB repair ($DSBD_{10}$ = 118), whereas *E. coli* ($DSBD_{10}$ = 6) and *P. putida* ($DSBD_{10}$ = 5) are the least efficient, with the others arranged between these extremes. It is useful to emphasize that, as reported, the extremely high IR survival (D_{10}) of wild-type *D. radiodurans* is undiminished in the *D. radiodurans* MnSod-deficient mutant (*sodA*$^-$) growing under high-level chronic gamma radiation (50 Gy/h) or exposed to massive acute doses (12 kGy) (7, 15, 29) (Table 1); thus, this enzyme cannot be responsible for the high IR resistance of these cells.

Thirty-Five–Gigahertz EPR Measurements. To carry out EPR measurements of Mn^{2+} speciation and test for correlations with the measured IR survival (D_{10}) and repair efficiency ($DSBD_{10}$), cells for each member of the experimental panel (Table 1) were harvested at the middle- to late-exponential growth phase, and the 35-GHz (Q-band) absorption-display EPR spectra were collected from the intact, viable cells. We had previously found (15, 26) that the Q-band (35 GHz) continuous wave (CW) absorption-display EPR spectra, but not derivative spectra at X- or Q-bands (or, in fact, at any frequency), reveal that cellular Mn^{2+} exists as two distinct pools of Mn^{2+} complexes. First, as illustrated in Fig. 1, *Lower*, the g-2 region of the spectrum (~12 kG) is dominated by a narrow signal (<1 kG in width) associated with antioxidant H-Mn^{2+} complexes with simple

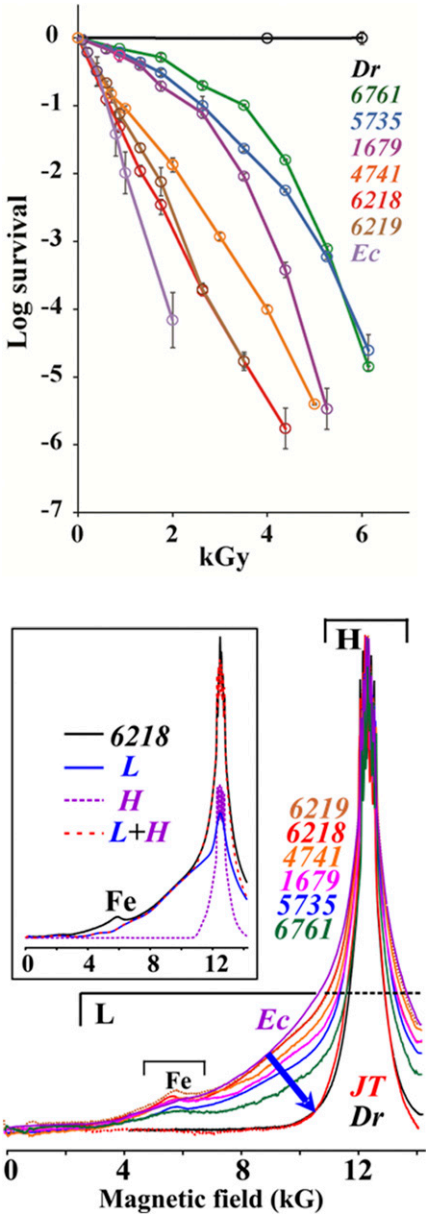

Fig. 1. Cellular IR survival and Mn speciation. (*Upper*) IR survival curves of indicated strains. Bacteria and yeasts were grown, irradiated to the indicated doses (kGy), and then quantified for survival by colony-forming unit assay (*SI Appendix, Materials and Methods*). Values are for three independent trials with SDs shown. Shoulders on cell survival curves correspond to dose-dependent changes in the efficiency/accuracy of enzymatic repair (5). (*Lower*) Thirty-five–gigahertz, 2-K, 100-kHz field-modulated rapid-passage absorption-display EPR spectra of selected bacteria/yeasts/human Jurkat T cells (*JT*), normalized to maximum height. "H" and "L" braces represent the field ranges over which H-Mn^{2+} and L-Mn^{2+} complexes contribute, the arrow indicates a monotonic decrease of the L-Mn^{2+} contribution (increasing f_H) with increasing D_{10} (Table 1, which contains strain abbreviations), *JT* as an apparent exception is discussed in main text, and Fe represents Fe(III) signals. Conditions were as follows: microwave frequency of 34.8–34.9 GHz, T = 2 K, scan time = 8 min, modulation amplitude = 2G. (*Inset*) Thirty-five–gigahertz EPR spectrum of *S. cerevisiae* strain EXF-6218, along with a simulation obtained by appropriately summing the contributions from simulations of exemplar spectra representing the H-Mn^{2+} and L-Mn^{2+} pools (f_H = 0.20); exemplar spectra were calculated as described in *SI Appendix, Materials and Methods*. Cells represented in both panels (*Upper* and *Lower*) were prepared the same way before analysis (*SI Appendix, Materials and Methods*). *Dr*, *D. radiodurans*; *Ec*, *E. coli*.

metabolites (e.g., orthophosphate), which displays a sextet pattern arising from hyperfine interactions with the ^{55}Mn (nuclear spin, I = 5/2) nucleus [hyperfine coupling, A ~ 90 G (30, 31)]. Then, this central H-feature "rides on" and is flanked by broad "wings" extending from fields of ~2 kG to fields well above the magnet limit, which are associated with a heterogeneous population of low-symmetry (L) Mn^{2+} complexes. The previous, limited observations further suggested to us the hypothesis that the relative amounts of the two pools might track with IR survival, D_{10}. In this regard, Mn^{2+} in *D. radiodurans* cells, which are extremely IR-resistant, exists almost exclusively as antioxidant H-complexes, whereas Mn^{2+} in *E. coli* cells, which are IR-sensitive, exists primarily as L-complexes (15). In vivo, H-Mn^{2+} complexes in bacteria protect proteins, but not DNA, from IR-induced ROS (7, 11, 18, 19); similarly, synthetic H-Mn^{2+} complexes provide strong in vitro protection of proteins, but not DNA, from ROS (11, 19–24). Moreover, H-Mn^{2+}–accumulating yeasts consistently display elevated ROS-scavenging capacities (Fig. 2, *Upper*) that protect proteins from gamma radiation (Fig. 2, *Lower*), but have no effect on IR-induced DSB yields (*SI Appendix*, Fig. S1 *C* and *D*).

Qualitative inspection of the absorption-display 35-GHz EPR spectra for bacteria and yeasts (Fig. 1, *Lower*) supports this hypothesis. In these normalized spectra, the intensity of the wings, which reflect the amount of L-Mn^{2+} relative to H-Mn^{2+}, monotonically decreases with increasing cellular IR survival as measured by D_{10} (Table 1). However, human Jurkat T cells are outliers, displaying a spectrum essentially identical to that of the paradigmatic IR-resistant bacterium, *D. radiodurans*, whereas its D_{10} value indicates extreme IR sensitivity (Fig. 1, *Lower* and Table 1). Below, we return to and resolve this apparent contradiction.

High-Frequency/High-Field EPR. As noted above, MnSod is not responsible for the high IR survival of wild-type *D. radiodurans* studied here, as the IR resistance is undiminished in the isogenic *D. radiodurans* MnSod-deficient mutant (*sodA*$^-$), as reported earlier (7, 10, 15, 17) and confirmed here (Table 1). Nonetheless, in consideration of reports based on high-frequency/high-field (HFHF) EPR spectroscopy that Mn^{2+}Sod is abundant, and indeed critical in the IR survival of *D. radiodurans*, rather than the H-Mn^{2+} complexes (32), we used HFHF derivative-display EPR spectroscopy (33) (*SI Appendix, Materials and Methods*) to determine the amount of Mn^{2+}Sod present in the *D. radiodurans* strains. HFHF EPR is more sensitive to the presence of Mn^{2+}Sod (32) than 35-GHz spectroscopy, which gave no evidence of Mn^{2+}Sod (15). The spectrum of Mn^{2+}Sod collected at 321 GHz (*SI Appendix*, Fig. S4) shows sharp, but low-intensity, peaks across the g-2 region. In particular, it shows signature features to low and high fields of the typical ^{55}Mn sextet at g-2 that comprises the spectrum for the H-Mn^{2+} of *D. radiodurans* (*SI Appendix*, Fig. S4). Through use of simulations of the *D. radiodurans* Mn^{2+} and Mn^{2+}Sod spectra (*SI Appendix*, Fig. S5) to calibrate spectrum amplitudes, we find that Mn^{2+}Sod is present in negligible amounts, comprising, at most, ~5% of the total Mn^{2+} pool (*SI Appendix, Materials and Methods*). As XANES (X-ray absorption near-edge structure) measurements show an absence of cellular Mn^{3+} (11), the EPR measurements complement the survival measurements on the MnSod knockout strains by indicating that not only is Mn^{2+}Sod not responsible for the observed high cellular IR survival in these wild-type cells harvested in log phase (Table 1) but that, in fact, they contain little holo-MnSod of any kind. This is consistent with earlier HFHF measurements of MnSod populations in log phase (32). However, it was incorrectly concluded from the high MnSod population found in the late-stationary phase that MnSod is responsible for high cellular survival throughout the growth cycle (32). Earlier data for the *D. radiodurans* MnSod-deficient mutant (*DrsodA*$^-$) showed that this enzyme does not contribute to acute IR survival of log-phase cells. Although late-stationary-phase cells were not tested (15, 29),

Table 1. Values for prokaryotes and eukaryotes of the cell panel of the IR resistance indexes $DSBD_{10}$ (DSB repair efficiency) and D_{10} (survival), DSB yield, genome size, and the Mn^{2+} speciation index f_H, as assessed by EPR

Name	Short name	$DSBD_{10}$	D_{10}, kGy	DSB yield	GS, Mbp	f_H	Source
Bacteria							
D. radiodurans ATCC BAA-816	*Dr*	118	12.0	0.003	3.3	0.94	(5, 7)
D. radiodurans sodA$^-$	*Dr sodA*$^-$	118	12.0	0.003	3.3	0.94	(5, 15)
D. geothermalis DSM 11300	*Dg*	118	12.0	0.003	3.3	0.94	(7)
D. ficus KS 0460	*Df*	84	7.0	0.003	4.0	0.97	(2, 7)
R. xylanophilus DSM 9941	*Rx*	59	6.0	0.003	3.3	0.97	(46)
A. radioresistens MD929, USU	*Ar*	48	5.0	0.003	3.2	0.7	(This study)
E. faecium ATCC 19434	*Ef*	18	2.0	0.003	3.0	0.81	(7)
E. coli K-12, MG1655	*Ec*	6	0.7	0.002	4.6	0.17	(5, 7)
P. putida ATCC 47054	*Pp*	5	0.3	0.003	6.1	0.13	(5, 7)
Human cells							
Jurkat T4 human cells ATCC TIB-152	*JT*	72	0.004	0.006	3,000	0.95	(27, 28)
Archaea							
H. salinarum ATCC 700922	*Hs*	39	5.0	0.003	2.6	0.95	(43, 45)
H. volcanii DS-70	*Hv*	18	1.5	0.003	4.0	0.84	(43, 45)
Yeasts							
S. cerevisiae EXF-6761	*6761*	32	3.5	0.0009	10	0.51	(Fig. 1, *Upper* and *SI Appendix*, Fig. S1)
S. cerevisiae EXF-5735	*5735*	20	2.6	0.00075	10	0.3	(Fig. 1, *Upper* and *SI Appendix*, Fig. S1)
S. cerevisiae FY1679	*1679*	20	2.4	0.0007	12	0.26	(Fig. 1 *Upper* and *SI Appendix*, Fig. S1)
R. taiwanensis MD1149, USU	*Rt*	16	0.8	0.001	20	0.35	(This study)
S. cerevisiae BY4741	*4741*	10	1.0	0.0008	12	0.21	(Fig. 1, *Upper* and *SI Appendix*, Fig. S1)
S. cerevisiae BY4741, *sod1*$^-$	*Sc sod1*$^-$	10	1.4	0.0008	12	0.21	(This study)
S. cerevisiae BY4741, *sod2*$^-$	*Sc sod2*$^-$	10	1.1	0.0008	12	0.21	(This study)
S. cerevisiae EXF-6219	*6219*	7	0.8	0.0006	14	0.23	(Fig. 1, *Upper* and *SI Appendix*, Fig. S1)
S. cerevisiae EXF-6218	*6218*	8	0.8	0.00075	14	0.2	(Fig. 1, *Upper* and *SI Appendix*, Fig. S1)

Tabulated quantities: D_{10}, dose at 10% survival (kGy); $DSBD_{10}$ = [D_{10} (Gy)] × [DSB Yield (DSB/Mbp/Gy)] × [Genome Size (Mbp)], DSBs per haploid genome; DSB yield (DSB/Mbp/Gy). Gamma-radiation–induced cellular DSB damage is linear with dose, with DSB yields falling within narrow ranges: for circular genomes of prokaryotes (0.002 ± 0.001 DSB/Mbp/Gy), for linear genomes of animal cells (0.006 ± 0.002 DSB/Mbp/Gy), and for linear genomes of yeasts (0.0006 ± 0.0003 DSB/Mbp/Gy) (2, 5, 7, 27) (*SI Appendix*, Fig. S1). Estimated uncertainties for f_H are <5% (*SI Appendix, Materials and Methods*). The source column lists citations for IR-induced DSB yields and genome sizes. f_H, fraction of H-Mn^{2+}; GS, genome size (Mbp); USU, Uniformed Services University.

we furthermore note that *DrsodA*$^-$ displays luxuriant growth on solid medium under high-level chronic IR (50 Gy/h, ^{137}Cs) irrespective of the growth stage of inoculated cells (7). Moreover, *E. coli sodA*$^-$ (14) and yeast *sod*$^-$ mutants (Table 1) are as IR-resistant, if not more resistant, than the wild types. Finally, the earlier HFHF work reported only the central portion of the MnSod spectrum, as in *SI Appendix*, Fig. S4 (32); for completeness, collection and analysis of the full Mn^{2+}Sod spectrum here (*SI Appendix*, Fig. S6) now confirm the reported magnitudes of the parameters that define the EPR spectrum of MnSod [the so-called zero-field splitting (ZFS) parameters], and further yield the sign of the dominant parameter (23, 24) (*SI Appendix, Materials and Methods*).

Correlation of IR Sensitivity and EPR. To quantify the correlation between increasing IR survival and an increasing population of H-Mn^{2+} complexes revealed in Fig. 1, *Upper* and *Lower*, a simple "quantitation by simulation" procedure (34, 35) using the EasySpin program (36) was developed to decompose the cellular Mn^{2+} 35-GHz absorption-display EPR spectra into fractional contributions from spectra that represent the L- and H-pools (*SI Appendix, Materials and Methods*). The contribution of the H-Mn^{2+} pool to the EPR spectrum of a cell type was modeled as an optimized sum of a simulated exemplar spectrum that corresponds to that of the Pi complex of Mn^{2+} (*SI Appendix*, Fig. S2; denoted H′) and of a simulated exemplar spectrum corresponding to that of Mn^{2+} with bound imidazole (*SI Appendix*, Fig. S2; denoted H″); the presence of an H″ contribution is generally required when H-Mn^{2+} is dominant. Guided by our recent experience with the EPR of Mn^{2+} complexes (37), we model the broad features contributed by the heterogeneous cellular L-Mn^{2+} pool with a single exemplar spectrum (*SI Appendix*, Fig. S2) in which the parameters that govern the breadth of an Mn^{2+} spectrum (ZFS parameters) (30, 31) are larger and more widely distributed than those for H-Mn^{2+} (*SI Appendix, Materials and Methods*). For each cell type, these exemplars are then summed in proportions that yield a match to the experimental spectrum. The total fraction of the H-Mn^{2+} contribution is given by the sum of the fractional contributions of the H-exemplars, $f_H = f_{H'} + f_{H''}$; the cellular L-Mn^{2+} pool then has a fraction, $f_L = 1 - f_H$. An example of a two-component decomposition (H = H′, L) is shown for yeast strain EXF-6218, for which $f_H = 0.20$ (Fig. 1, *Lower Inset*). *SI Appendix*, Fig. S3 shows the decomposition of the Jurkat T cell spectrum, for which $f_H = 0.95$ and which required a contribution from H″. Table 1 lists the f_H for each cell type studied. As an illustration of the range of speciation observed for the cell panel under normal growth conditions (Table 1), the Mn^{2+} of *D. radiodurans* and Jurkat cells is associated almost exclusively with H-Mn^{2+} complexes, $f_H \sim 0.95$, whereas *E. coli* represents an opposite extreme, with a dominant population of L-Mn^{2+} complexes: $f_H = 0.17$, $f_L = 0.83$.

Fig. 3 and *SI Appendix*, Fig. S7 display several alternative forms of a plot of the variation of the fraction of high-symmetry, f_H, Mn^{2+} complexes in cells that have not undergone IR exposure, as a function of the IR DNA repair efficiency index, $DSBD_{10}$, for the cell-type panel (Table 1). *SI Appendix*, Fig. S7 shows that f_H correlates with $DSBD_{10}$ in a manner suggestive of an "IR resistance/binding isotherm" (31), with f_H rising rapidly with increasing $DSBD_{10}$ from its lowest value, $f_H = 0.13$ at $DSBD_{10} = 5$ (*P. putida*; Table 1) to $f_H \gtrsim 0.9$ for $DSBD_{10} \gtrsim 60$, and then essentially saturating thereafter. Such an isotherm is conveniently linearized in a "Hill plot" (38) of the EPR speciation, which plots the logarithm of the ratio of the fractional populations of H- and L-pools of Mn^{2+} [$f_H/f_L = f_H/(1 - f_H)$] against the logarithm of

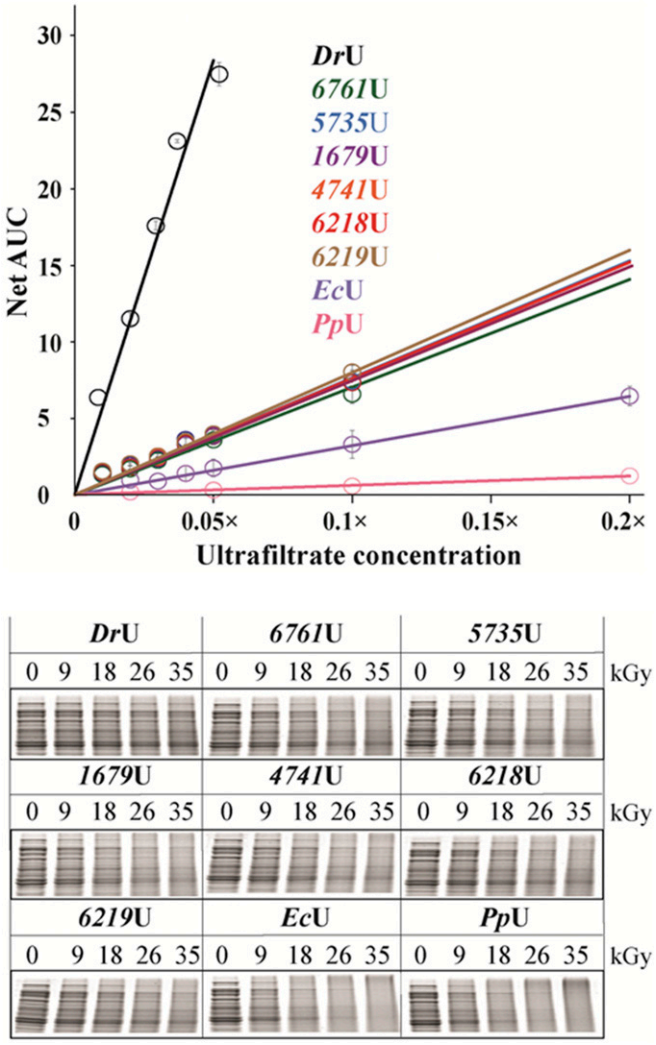

Fig. 2. Antioxidant capacity of LMW extracts (U, ultrafiltrates) of bacteria (e.g., *Pp*U) and yeasts (e.g., *6761*U). (*Upper*) ROS-scavenging capacity of U assessed by oxygen radical absorbance capacity assay (47, 48). Net AUC, net area under the fluorescence decay curve. The U's were diluted to 0.01×, 0.02×, 0.03×, 0.04×, 0.05×, 0.1×, or 0.2× for the assay. (*Lower*) Capacity of U of the indicated strains to protect proteins during gamma irradiation. Indicated U's were mixed with purified *E. coli* proteins, irradiated to the indicated doses (kGy), and assayed for protein damage (e.g., strand breaks, cross-links), manifest as smears. *Dr*U, *D. radiodurans* ultrafiltrates; *Ec*U, *E. coli* ultrafiltrates; *Pp*U, *P. putida* ultrafiltrates.

$DSBD_{10}$. Such a plot (Fig. 3) indeed exhibits the strong linear correlation expected for an IR resistance/binding isotherm (*SI Appendix, Materials and Methods*; Pearson correlation coefficient = 0.883, $P = 5.50 \times 10^{-7}$; Spearman rank correlation coefficient = 0.849, $P = 4.25 \times 10^{-6}$). Conversely, this correlation over a range, $5 \lesssim DSBD_{10} \lesssim 118$ implies that the speciation in live cells, the fraction of antioxidant H-Mn^{2+} as captured by the EPR-derived index f_H, is a powerful predictor of the index of DSB repair efficiency, $DSBD_{10}$, which is based on survival as controlled for the genome size of the organism.

Below, we consider possible implications of this and other alternative correlations between properties of intracellular Mn^{2+} and IR resistance. We first note that Fig. 3 shows that D_{10} is a suitable IR survival metric at the organism level (e.g., yeasts), which naturally scales with genome size. The figure further provides evidence that $DSBD_{10}$, instead, is the proper metric of IR resistance at the molecular level. In other words, the survival index, D_{10}, is a suitable measure of IR resistance only for cells of similar genome size, and for such cells, the speciation from EPR is roughly correlated with D_{10} (Fig. 3, *Inset*), as expected, although not as well correlated as with $DSBD_{10}$ (Fig. 3). However, comparing the use of these two IR tolerance measures for the human Jurkat cells clearly distinguishes between them. The Mn^{2+} EPR phenotype for Jurkat cells is "high H-Mn^{2+}," namely, high f_H (Fig. 1, *Lower*), implying high DSB repair efficiency, which is in excellent correspondence with their $DSBD_{10}$ (Fig. 3). However, in the Hill plot of f_H versus the IR survival index (D_{10}), the Jurkat cells are hugely off the correlation shown by the other cells (Fig. 3, *Inset*) because the extremely low D_{10} index of the Jurkat cells does not account for the large Jurkat genome, and therefore the total number of DSBs, which scales with genome size. Thus, the two plots in Fig. 3 demonstrate the genome size-based limitations of D_{10} as a molecular measure of IR resistance. Overall, Fig. 3 shows that for all domains of life, over a range of thousands of grays, the Mn^{2+} speciation within non-irradiated viable cells as determined by absorption-display EPR, f_H, has high predictive value for DSB repair efficiency, as measured by the $DSBD_{10}$, and thus for resistance to IR exposure.

Molecular Interpretation. Consistent with our earlier results (7), *SI Appendix*, Fig. S8, *Left* shows that there is, at best, a loose correlation between $DSBD_{10}$ and total cellular Mn concentration, [Mn]; namely, the figure shows a broad cluster of points for cells with high [Mn] and high $DSBD_{10}$, and, similarly, for cells with low values for both. *SI Appendix*, Fig. S8, *Right* shows a more significant correlation between the total H-Mn concentration, [H-Mn] = f_H [Mn], but the correlation is poorer than that between f_H itself and $DSBD_{10}$, as revealed in Fig. 3 and *SI Appendix*, Fig. S7. This difference may well reflect, in some part, imprecise values for [Mn], which are determined from the number of Mn ions per cell, as measured by inductively coupled plasma MS, and an average cell volume, an imprecision that translates to [H-Mn] (*SI Appendix*, Table S2). Regardless, at this stage, in considering IR resistance it is most revealing to focus on f_H; future improvements in the concentration measurements may allow a refinement of this approach.

A molecular interpretation of the isotherm/Hill plot correlation between the EPR and $DSBD_{10}$ measures emerges from a simple

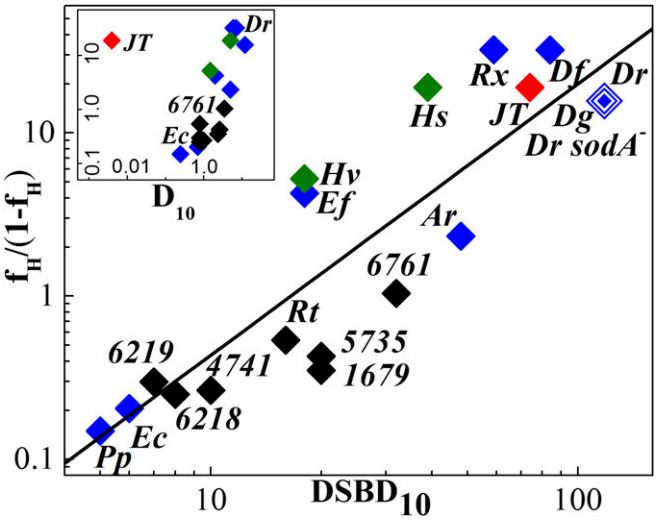

Fig. 3. Correlation between IR resistance ($DSBD_{10}$) and EPR speciation, f_H, plotted as the logarithm of the ratio $f_H/f_L = f_H/(1 - f_H)$ against the logarithm of $DSBD_{10}$. Symbols are as follows: bacteria (*blue*), yeasts (*black*), archaea (*green*), Jurkat T cells (*JT*; *red*). The straight line represents a fit to the Hill equation (Eq. **3b**) as discussed in *SI Appendix, Materials and Methods*. The robustness of this correlation is discussed in *SI Appendix* and summarized in the main text. (*Inset*) Analogous plot of speciation versus D_{10}.

heuristic analysis of ligand binding by intracellular Mn^{2+} (*SI Appendix*, *Materials and Methods*). Guided by the decomposition of the cellular EPR spectra into contributions from two pools (Fig. 1, *Lower*, *Inset*), we first divide Mn^{2+} complexes and their ligands into two types, H and L, with H representing an "average" H′/H″-ligand. We further assume that n H-ligands compete with n L-ligands for binding to the cellular Mn^{2+}. In all cell types, the concentration of Mn^{2+} is much less than the concentration of either ligand type, which ensures that there is a negligible amount of free Mn^{2+}. For example, under standard growth conditions, *D. radiodurans* accumulates ~10^5 Mn atoms per cell (7, 11, 15, 19), but millimolar concentrations of Mn-binding LMW ligands (e.g., peptides, orthophosphate) (19). Under these circumstances, the relative binding strengths of the populations of H- and L-ligands are simply represented by the product, $K_i(C_i)^n$, i = H, L (H_2O ligands not explicitly denoted), where K_i and C_i, respectively, are the effective binding constants and concentrations of ligand type i = H, L (*SI Appendix*, *Materials and Methods*). This results in a binding isotherm (38) that relates f_H to the ratio of ligand concentrations, C_H/C_L (Eq. **1** and *SI Appendix*, Eq. **S3**):

$$f_H\left(\frac{C_H}{C_L}\right)=\frac{K_{HL}\left(\frac{C_H}{C_L}\right)^n}{1+K_{HL}\left(\frac{C_H}{C_L}\right)^n};\quad K_{HL}=\frac{K_H}{K_L}. \qquad [1]$$

As the key step that correlates IR resistance with Mn^{2+} speciation, we assign the $DSBD_{10}$ index as corresponding to (proportional to) the ratio of the concentrations of the ligand types,

$$DSBD_{10}\propto\frac{C_H}{C_L}, \qquad [2]$$

which results (*SI Appendix*, *Materials and Methods*) in an "IR resistance isotherm" that relates f_H to $DSBD_{10}$,

$$f_H=\frac{\kappa(DSBD_{10})^n}{1+\kappa(DSBD_{10})^n}, \qquad [3a]$$

as suggested above, where κ represents the product of the ratio, $K_{HL}=K_H/K_L$, with the proportionality constant implied by Eq. **2**. The validity of this treatment is highlighted by rewriting Eq. **3a** as a linearized "Hill equation" (38),

$$\log\left(\frac{f_H}{1-f_H}\right)=n\log(DSBD_{10})+\log(\kappa), \qquad [3b]$$

which precisely corresponds to the form of the correlation revealed by the plot in Fig. 3. The excellent representation of the data by Eq. **3b** (Fig. 3) shows that the microscopic interpretation of $DSBD_{10}$ through Eq. **2** nicely describes the correlation between IR resistance and EPR-determined speciation. A strong association between the EPR-derived metric f_H and the DSB repair efficiency metric $DSBD_{10}$ is supported by detailed statistical analysis presented in *SI Appendix*. Specifically, linear regression of $\log[DSBD_{10}]$ (y axis) versus $\log[f_H/(1-f_H)]$ (x axis) produced a coefficient of determination of $R^2=0.78$, suggesting that $\log[f_H/(1-f_H)]$ explains 78% of the variance in $\log[DSBD_{10}]$. To view f_H as a predictor of IR resistance, $DSBD_{10}$, one needs only invert Eq. **3b**,

$$\log(DSBD_{10})=\left(\frac{1}{n}\right)\log\left(\frac{f_H}{1-f_H}\right)-\log(\kappa)/n, \qquad [4]$$

and permute the axes of Fig. 3.

With this molecular interpretation of $DSBD_{10}$ (Eq. **2**), the meaning of the experimental correlation of Fig. 3 becomes clear: For nutrient-replete cells that have a sufficient amount of Mn^{2+}, $DSBD_{10}$ directly correlates with the ratio of the concentrations of the H- and L-ligands (Eq. **2**), which, in turn, determines the speciation of the cellular Mn^{2+} (Eq. **3**). Monte Carlo simulation confirms the robustness of the correlation between $\log[f_H/(1-f_H)]$ and $\log[DSBD_{10}]$, taking into account realistic error distributions and magnitudes for both of these variables (*SI Appendix*, *Materials and Methods*). In the most IR-resistant organisms, such as *Deinococcus* and *Rubrobacter* spp., the binding strength of the H-ligands far exceeds that of the L-ligands. The H-ligands overwhelmingly outcompete any L-ligands present, including the aposuperoxide dismutase polypeptide if present, driving the Mn^{2+} speciation to near-quantitative existence as LMW, IR-protective H-Mn^{2+} complexes ($f_H\rightarrow 1$). The observations reported here thus imply that in Mn^{2+}- and nutrient-replete cells, the antioxidant H-Mn^{2+} complexes, as quantified by absorption-display EPR spectroscopy, govern IR survival in yeasts, archaea, bacteria, and human cells, but not influenced by antioxidant enzymes, namely, MnSod. This indicator of Mn^{2+} speciation will be further strengthened with a widened panel of cell-type calibrants, studies of how f_H changes during cell growth and aging, and further refinement of the EPR spectroscopic approach, as well as its complementation by electron-nuclear double-resonance studies (15, 26). In particular, human cells and their cancer cell counterparts can display large differences in their IR sensitivities (6), and the H-Mn^{2+} content may provide a suitable metric to determine dosing regimens for different cancer types during radiation therapy (Fig. 3).

Discussion

We have revealed that in Mn- and nutrient-replete cells, the fraction of antioxidant metabolite complexes of Mn^{2+}, the H-Mn^{2+}, as captured by the EPR-derived index f_H, strongly correlates with the DSB repair efficiency index, $DSBD_{10}$ (Fig. 3, Eqs. **2** and **3**, and *SI Appendix*, *Materials and Methods*). This strong association is remarkable, considering the vast differences in taxonomic status, genome size, and radioresistance between studied cell types. In contrast, the antioxidant enzyme MnSod plays a negligible part in IR survival in such cells (7, 9, 10, 14–16), as confirmed here. The cellular content of H-Mn^{2+} complexes is now the strongest biological indicator of cellular IR resistance between and within organisms representing the three domains of life.

That MnSod confers no discernible advantage over the H-Mn^{2+} complexes for IR survival (Table 1) is expected from earlier studies (7, 9, 10, 14–16). Metal-bound MnSod is dispensable for IR resistance (Table 1), and indeed is shown here to be absent or nearly so (*SI Appendix*, Fig. S4) in log-phase *D. radiodurans* cells with extremely high IR survival. These findings suggest that in nutrient-replete organisms, H-Mn^{2+} complexes govern IR/ROS resistance. This dominant role of H-Mn^{2+} in IR resistance of such cells further implies that MnSod may be more important under nutrient-limited conditions, when Mn^{2+} and Pi are in lower abundance and the organic ligands (e.g., free amino acids, peptides, nucleosides) of H-Mn^{2+} complexes are consumed, typically in rapidly dividing cells or following starvation in aging cells (7, 39).

This study has extended insights on the role of Mn antioxidants in the IR survival (D_{10}) of bacteria (see Introduction) to a group of simple eukaryotes by showing that variations in D_{10} and efficiency of DNA repair ($DSBD_{10}$) among nine bacteria and nine yeasts are strongly correlated to their H-Mn^{2+} (f_H) content (Table 1). Importantly, we also show that the IR resistance of *S. cerevisiae* is not affected by the presence or absence of Sod enzymes, whether the major Cu/Zn-dependent SOD1, which is localized throughout the cell, or the Mn-dependent SOD2, which is only in the mitochondrial matrix (Table 1). Also consistent with this analysis, IR-induced DSB yields in *S. cerevisiae* genomes (0.0006–0.0009 DSB/Mbp/Gy) (*SI Appendix*, Fig. S1) are similar to those reported in other organisms; IR-induced DSB yields across representative archaea, bacteria, and animal cells fall within a narrow range (0.001–0.005 DSB/Mbp/Gy) (5) (Table 1).

Based on the number and diversity of yeasts we examined (*SI Appendix*, Table S1), our results elevate many environmental yeasts to the class of biology's most radiation-resistant organisms. We believe the ability of EPR to accurately measure differences in the IR survival between numerous phylogenetically distinct yeast strains of similar genome size makes paramagnetic spectroscopy suitable for gauging the IR resistance of other eukaryotic cell types, including cancer cells.

In the case of *D. radiodurans*, we note that the $\sim 10^5$ Mn^{2+} ions accumulated per cell are not uniformly distributed (7, 11). Rather, Mn is most concentrated in granules, often colocalized with the DNA-containing nucleoid (11, 39), providing further support to the proposed Mn antioxidant role in repair of IR-induced DSBs, the most consequential form of DNA damage (5). These granules could serve as primitive antioxidant organelle-like structures, strengthening the antioxidant protection in the proximity of the genome, where functional DNA repair and replication proteins are needed most.

While the existence of high cellular content of H-Mn^{2+} complexes appears in species across archaea, bacteria, and eukaryotes, many microbes can survive vastly greater IR doses than they ever would have experienced in their natural environment over geological times. It therefore seems likely that the underlying metabolic systems for the accumulation of antioxidant H-Mn^{2+} complexes evolved not as a response to IR but, instead, in response to other severe oxidative pressures that diminish proteome functionality (17): desiccation, UV light, aging, and other stressors. Gauging the antioxidant capacity of cells by EPR may thus have applications beyond radiobiology.

Materials and Methods

Strains. Bacteria used in this study were as follows: *D. radiodurans* [American Type Culture Collection (ATCC) BAA-816], *D. radiodurans* (*sodA*$^-$) (29), *D. geothermalis* [Deutsche Sammlung von Mikroorganismen (DSM) 11300], *D. ficus* KS0460 (EXB L-1957) (2), *R. xylanophilus* (DSM 9941), *A. radioresistens* [MD929; Uniformed Services University of the Health Sciences (USUHS)], *E. faecium* (ATCC 19434), *E. coli* (strain K-12; MG1655), and *P. putida* (ATCC 47054). Yeasts used in this study (eight *S. cerevisiae* strains and one *Rhodotorula* strain) examined by EPR were chosen from a collection of fungi gauged for IR resistance (D_{10}) (Table 1 and *SI Appendix*, Table S1): *S. cerevisiae* (*6761*) (EXF-6761; diploid), *S. cerevisiae* (*5735*) (EXF-5735; diploid), *S. cerevisiae* (*1679*) (FY1679; diploid) (40), *S. cerevisiae* (*6219*) (EXF-6219; diploid), *S. cerevisiae* (*6218*) (EXF-6218; diploid), *S cerevisiae* (*4741*) (BY4741; haploid) (41), *S. cerevisiae* (*Scsod1*$^-$) (BY4741-ΔSOD1; haploid) (42), *S. cerevisiae* (*Scsod2*$^-$) (BY4741-ΔSOD2; haploid) (42), and *R. taiwanensis* (MD1149; USUHS; accession number: PRJNA352283). Archaea used in this study were *H. salinarum* (ATCC 700922Δura3) (43) and *H. volcanii* (DS-70). Human cells used in this study were Jurkat T cells (ATCC TIB-152).

More information about growth, acute ^{60}Co irradiations, ultrafiltrates, intracellular antioxidant capacity of ultrafiltrates, PFGE, and Monte Carlo simulation is provided in *SI Appendix, Materials and Methods*.

EPR. As reported (37), cryogenic (2 K) Q-band (35 GHz) CW, 100-kHz field-modulated, dispersion-mode, rapid-passage absorption-display EPR spectra were collected on a spectrometer previously described (44). HFHF EPR spectra were recorded on a laboratory-built spectrometer at the EMR facility of the National High Magnetic Field Laboratory (33) (*SI Appendix*).

ACKNOWLEDGMENTS. We thank Prof. Valeria Culotta for supplying *sod*$^-$ *S. cerevisiae* strains and Michael Woolbert (USUHS) for assistance in irradiator maintenance and calibration. This study was supported by NIH Grant GM111097 (to B.M.H.) and by funds received from Defense Threat Reduction Agency (DTRA) Grant HDTRA1620354 (to M.J.D.), DTRA Grant HDTRA1-15-1-0058 (to I.S.), and Grant FA9550-14-1-0118 (to J.D.) from the Air Force Office of Scientific Research (AFOSR). High-field EPR spectra were recorded at the NHMFL, which is funded by the National Science Foundation through Cooperative Agreement DMR-1157490 between the State of Florida and the US Department of Energy. The funders had no role in study design, data collection and analysis, decision to publish, or preparation of the manuscript. The opinions expressed herein are those of the author(s), and are not necessarily representative of those of the USUHS; DTRA; AFOSR; the Department of Defense; or the US Army, Navy, or Air Force.

1. Makarova KS, et al. (2001) Genome of the extremely radiation-resistant bacterium *Deinococcus radiodurans* viewed from the perspective of comparative genomics. *Microbiol Mol Biol Rev* 65:44–79.
2. Matrosova VY, et al. (2017) High-quality genome sequence of the radioresistant bacterium *Deinococcus ficus* KS 0460. *Stand Genomic Sci* 12:46.
3. Harris DR, et al. (2009) Directed evolution of ionizing radiation resistance in *Escherichia coli*. *J Bacteriol* 191:5240–5252.
4. Yard BD, et al. (2016) A genetic basis for the variation in the vulnerability of cancer to DNA damage. *Nat Commun* 7:11428.
5. Daly MJ (2012) Death by protein damage in irradiated cells. *DNA Repair (Amst)* 11:12–21.
6. Scott JG, et al. (2017) A genome-based model for adjusting radiotherapy dose (GARD): A retrospective, cohort-based study. *Lancet Oncol* 18:202–211.
7. Daly MJ, et al. (2004) Accumulation of Mn(II) in *Deinococcus radiodurans* facilitates gamma-radiation resistance. *Science* 306:1025–1028.
8. Daly MJ (2009) A new perspective on radiation resistance based on *Deinococcus radiodurans*. *Nat Rev Microbiol* 7:237–245.
9. Archibald FS, Fridovich I (1981) Manganese and defenses against oxygen toxicity in Lactobacillus plantarum. *J Bacteriol* 145:442–451.
10. Culotta VC, Daly MJ (2013) Manganese complexes: Diverse metabolic routes to oxidative stress resistance in prokaryotes and yeast. *Antioxid Redox Signal* 19:933–944.
11. Daly MJ, et al. (2007) Protein oxidation implicated as the primary determinant of bacterial radioresistance. *PLoS Biol* 5:e92.
12. Barnese K, Gralla EB, Valentine JS, Cabelli DE (2012) Biologically relevant mechanism for catalytic superoxide removal by simple manganese compounds. *Proc Natl Acad Sci USA* 109:6892–6897.
13. Barnese K, et al. (2010) Investigation of the highly active manganese superoxide dismutase from *Saccharomyces cerevisiae*. *J Am Chem Soc* 132:12525–12527.
14. Scott MD, Meshnick SR, Eaton JW (1989) Superoxide dismutase amplifies organismal sensitivity to ionizing radiation. *J Biol Chem* 264:2498–2501.
15. Sharma A, et al. (2013) Responses of Mn^{2+} speciation in *Deinococcus radiodurans* and *Escherichia coli* to γ-radiation by advanced paramagnetic resonance methods. *Proc Natl Acad Sci USA* 110:5945–5950.
16. Robinson CK, et al. (2011) A major role for nonenzymatic antioxidant processes in the radioresistance of *Halobacterium salinarum*. *J Bacteriol* 193:1653–1662.
17. Slade D, Radman M (2011) Oxidative stress resistance in *Deinococcus radiodurans*. *Microbiol Mol Biol Rev* 75:133–191.
18. Krisko A, Radman M (2010) Protein damage and death by radiation in *Escherichia coli* and *Deinococcus radiodurans*. *Proc Natl Acad Sci USA* 107:14373–14377.
19. Daly MJ, et al. (2010) Small-molecule antioxidant proteome-shields in *Deinococcus radiodurans*. *PLoS One* 5:e12570.
20. Berlett BS, Levine RL (2014) Designing antioxidant peptides. *Redox Rep* 19:80–86.
21. Peana M, et al. (2016) Manganese binding to antioxidant peptides involved in extreme radiation resistance in *Deinococcus radiodurans*. *J Inorg Biochem* 164:49–58.
22. Gayen M, et al. (2017) *Deinococcus* $Mn^{(2+)}$-peptide complex: A novel approach to alphavirus vaccine development. *Vaccine* 35:3672–3681.
23. Gaidamakova EK, et al. (2012) Preserving immunogenicity of lethally irradiated viral and bacterial vaccine epitopes using a radio- protective Mn^{2+}-Peptide complex from *Deinococcus*. *Cell Host Microbe* 12:117–124.
24. Gupta P, et al. (2016) MDP: A *Deinococcus* Mn^{2+}-decapeptide complex protects mice from ionizing radiation. *PLoS One* 11:e0160575.
25. Gladyshev E, Meselson M (2008) Extreme resistance of bdelloid rotifers to ionizing radiation. *Proc Natl Acad Sci USA* 105:5139–5144.
26. McNaughton RL, et al. (2010) Probing in vivo Mn(2+) speciation and oxidative stress resistance in yeast cells with electron-nuclear double resonance spectroscopy. *Proc Natl Acad Sci USA* 107:15335–15339.
27. Rothkamm K, Löbrich M (2003) Evidence for a lack of DNA double-strand break repair in human cells exposed to very low x-ray doses. *Proc Natl Acad Sci USA* 100:5057–5062.
28. Chatterjee P, et al. (2013) Defective chromatin recruitment and retention of NHEJ core components in human tumor cells expressing a Cyclin E fragment. *Nucleic Acids Res* 41:10157–10169.
29. Markillie LM, Varnum SM, Hradecky P, Wong KK (1999) Targeted mutagenesis by duplication insertion in the radioresistant bacterium *Deinococcus radiodurans*: Radiation sensitivities of catalase (katA) and superoxide dismutase (sodA) mutants. *J Bacteriol* 181:666–669.
30. Magnusson OT, Reed GH, Frey PA (1999) Spectroscopic evidence for the participation of an allylic analogue of the 5′-deoxyadenosyl radical in the reaction of lysine 2,3-aminomutase. *J Am Chem Soc* 121:9764–9765.
31. Reed GH, Markham GD (1984) EPR of Mn(II) complexes with enzymes and other proteins. *Biological Magnetic Resonance*, eds Berliner LI, Reuben J (Plenum, New York), Vol 6, pp 73–142.
32. Bruch EM, de Groot A, Un S, Tabares LC (2015) The effect of gamma-ray irradiation on the Mn(II) speciation in *Deinococcus radiodurans* and the potential role of Mn(II)-orthophosphates. *Metallomics* 7:908–916.
33. Hassan AK, et al. (2000) Ultrawide band multifrequency high-field EMR technique: A methodology for increasing spectroscopic information. *J Magn Reson* 142:300–312.
34. Stoll S (2014) Computational modeling and least-squares fitting of EPR spectra. *Multifrequency Electron Paramagnetic Resonance: Data and Techniques*, ed Misra SK (Wiley-VCH, Weinheim, Germany), 1st Ed, pp 69–138.

35. Yang AS, Gaffney BJ (1987) Determination of relative spin concentration in some high-spin ferric proteins using E/D-distribution in electron paramagnetic resonance simulations. *Biophys J* 51:55–67.
36. Stoll S, Schweiger A (2006) EasySpin, a comprehensive software package in spectral simulation and analysis in EPR. *J Magn Reson* 178:42–55.
37. Horitani M, et al. (2017) ^{13}C ENDOR spectroscopy of lipoxygenase-substrate complexes reveals the structural basis for C-H activation by tunneling. *J Am Chem Soc* 139: 1984–1997.
38. van Holde KE, et al. (2005) *Principles of Physical Biochemistry* (Prentice Hall, Englewood Cliffs, NJ), 2nd Ed.
39. Ghosal D, et al. (2005) How radiation kills cells: Survival of *Deinococcus radiodurans* and *Shewanella oneidensis* under oxidative stress. *FEMS Microbiol Rev* 29:361–375.
40. Winston F, Dollard C, Ricupero-Hovasse SL (1995) Construction of a set of convenient *Saccharomyces cerevisiae* strains that are isogenic to S288C. *Yeast* 11:53–55.
41. Brachmann CB, et al. (1998) Designer deletion strains derived from *Saccharomyces cerevisiae* S288C: A useful set of strains and plasmids for PCR-mediated gene disruption and other applications. *Yeast* 14:115–132.
42. Reddi AR, Culotta VC (2011) Regulation of manganese antioxidants by nutrient sensing pathways in *Saccharomyces cerevisiae*. *Genetics* 189:1261–1270.
43. Kottemann M, Kish A, Iloanusi C, Bjork S, DiRuggiero J (2005) Physiological responses of the halophilic archaeon *Halobacterium* sp. strain NRC1 to desiccation and gamma irradiation. *Extremophiles* 9:219–227.
44. Werst MM, Davoust CE, Hoffman BM (1991) Ligand spin densities in blue copper proteins by Q-band proton and nitrogen-14 ENDOR spectroscopy. *J Am Chem Soc* 113: 1533–1538.
45. Kish A, et al. (2009) Salt shield: Intracellular salts provide cellular protection against ionizing radiation in the halophilic archaeon, *Halobacterium salinarum* NRC-1. *Environ Microbiol* 11:1066–1078.
46. Ferreira AC, et al. (1999) Characterization and radiation resistance of new isolates of *Rubrobacter radiotolerans* and *Rubrobacter xylanophilus*. *Extremophiles* 3: 235–238.
47. Dávalos A, Bartolomé B, Suberviola J, Gómez-Cordovés C (2003) ORAC-fluorescein as a model for evaluating antioxidant activity of wines. *Pol J Food Nutr Sci* 12: 133–136.
48. Mikami I, Yamaguchi M, Shinmoto H, Tsushida T (2009) Development and validation of a microplate-based β-carotene bleaching assay and comparison of antioxidant activity (AOA) in several crops measured by β-carotene bleaching, DPPH and ORAC assays. *Food Sci Technol Res* 15:171–178.